Chemical Science

ROYAL SOCIETY OF CHEMISTRY

EDGE ARTICLE

View Article Online
View Journal | View Issue

Cite this: *Chem. Sci.*, 2026, **17**, 4256

All publication charges for this article have been paid for by the Royal Society of Chemistry

Spatial pinning of globally inert pores in a superhydrophobic hydrogen-bonded organic framework for inverse ethane/ethylene separation

Youlie Cai, [a] Jing-Hong Li, [b] Xiaoyan Xiao,[c] Runzhi Wei,[a] Rui-Biao Lin, *[b] Banglin Chen *[de] and Junkuo Gao *[a]

Overcoming the intrinsic polarity of hydrogen bonds to construct a C_2H_6-affinitive nonpolar pore environment using an entirely pore-oriented π-conjugated core presents a formidable challenge within hydrogen-bonded organic frameworks (HOFs). Herein, we propose a spatial pinning strategy for HOF pore construction. Hydrophobic molecular struts are pre-pinned within the precursor to restrict the conformational freedom of hydrogen-bonding arms, thereby governing framework stereochemistry, suppressing undesired π–π stacking, and generating four-way interconnected cavities between π-conjugated layers. Importantly, multiple interpenetrations shield polar hydrogen bonds, enabling a globally inert framework, as evidenced by an impressive contact angle exceeding 153° and an ultralow water vapor uptake of 0.057 g g^{-1}. Gas sorption experiments demonstrate a C_2H_6 adsorption capacity of 91.5 cm^3 g^{-1} and a C_2H_6/C_2H_4 selectivity of 2.0. Gas-loaded single crystals and theoretical calculations reveal that this globally inert pore environment profoundly enhances van der Waals forces between the host framework and C_2H_6, facilitating efficient gas packing. Furthermore, this HOF can produce high-purity C_2H_4 (>99.9%) from dynamic breakthrough experiments, with a maximum productivity of 36.0 L kg^{-1}. This work introduces a pivotal advancement in the precursor design strategy to precisely modulate secondary interaction mechanisms within porous organic frameworks, offering new horizons for customized pore engineering.

Received 3rd November 2025
Accepted 26th December 2025

DOI: 10.1039/d5sc08507a

rsc.li/chemical-science

Introduction

Ethylene (C_2H_4) is the cornerstone of the petrochemical industry, serving as a fundamental feedstock for numerous essential chemical products and intermediates.[1] With global production capacity reaching 228 million tons in 2023 and a projected average annual growth rate (AAGR) exceeding 6%, the demand for high-purity (≥99.9%) C_2H_4 is escalating.[2] Over 90% of C_2H_4 is produced *via* steam cracking, yielding a mixture rich in C_2H_4 and the byproduct ethane (C_2H_6). The stringent requirement for polymer-grade C_2H_4 necessitates a highly efficient separation process.[3] Currently, this separation is overwhelmingly accomplished *via* cryogenic distillation. However, the similar boiling points (~15 °C difference) and kinetic diameters (~0.28 Å difference) between C_2H_6 and C_2H_4 result in distillation accounting for up to 40% of energy consumption, alongside costly cryogenic equipment and operational expenses.[4] In this context, adsorptive separation using porous materials—particularly the development of C_2H_6-selective adsorbents—has emerged as a highly promising alternative strategy due to its potential for simplified operation and energy savings.[5]

Porous materials, including metal–organic frameworks (MOFs) and zeolites, have demonstrated impressive capabilities in this separation.[6–10] These adsorbents selectively capture one component over another by exploiting subtle differences in molecular size, polarity, or specific interactions such as π-complexation.[11,12] Nevertheless, a pervasive impediment to practical deployment lies in the inevitable presence of water vapor within the cracking gas.[13] Despite upstream dehydration processes, residual moisture persists. Such polar molecules readily interact with active sites and compete with the target gases for adsorption sites.[14,15] For size-exclusion-based

[a]*China-Uzbekistan Joint Laboratory on Advanced Porous Materials, State Key Laboratory of Bio-based Fiber Materials, School of Materials Science and Engineering, Zhejiang Sci-Tech University, Hangzhou, 310018, China. E-mail: jkgao@zstu.edu.cn*

[b]*Key Laboratory of Bioinorganic and Synthetic Chemistry of Ministry of Education, School of Chemistry, IGCME, Sun Yat-Sen University, Guangzhou, 510275, China. E-mail: linruibiao@mail.sysu.edu.cn*

[c]*State Key Laboratory of Silicon and Advanced Semiconductor Materials, School of Materials Science and Engineering, Zhejiang University, Hangzhou, 310027, China*

[d]*Fujian Provincial Key Laboratory of Polymer Materials, College of Chemistry and Materials Science, Fujian Normal University, Fuzhou, 350007, China. E-mail: banglin.chen@fjnu.edu.cn*

[e]*Key Laboratory of the Ministry of Education for Advanced Catalysis Materials, College of Chemistry and Materials Science, Zhejiang Normal University, Jinhua 321004, China*

adsorbents, water condenses into liquid films or clusters within micropores, impeding target gas access. Moreover, adsorbents exhibiting limited hydrolytic stability face the risk of structural degradation.[16–18] Overcoming this pervasive challenge thus necessitates a paradigm shift in material design, focusing on the creation of robust adsorbents with engineered water resistance and inherent hydrophobicity.

Over the past decade, hydrogen-bonded organic frameworks (HOFs) have emerged as an innovative class of porous materials for gas separation.[19–24] Carboxylic acid-based HOFs, distinguished by their highly directional hydrogen-bonded dimer motifs, constitute a key subclass.[25–37] Precursors containing aromatic rings facilitate the formation of hydrophobic frameworks, offering distinct advantages for achieving C_2H_6/C_2H_4 separation. Because C_2H_6 (44.7×10^{-25} cm^3) is more polarizable than C_2H_4 (42.5×10^{-25} cm^3),[38] nonpolar aromatic surfaces preferentially bind C_2H_6 through enhanced dispersion interactions while avoiding the electrostatic interactions associated with the quadrupole moment of C_2H_4. Indeed, several reported carboxylic acid-based HOFs leverage this principle, using precursors that direct benzene rings toward the pore surface to improve separation performance.[39–41] Nevertheless, the inherent polarity of carboxylic acid dimers as hydrogen bond donors/acceptors introduces hydrophilic domains on the pore surface. This hydrophilicity compromises C_2H_6 selectivity and curtails the potential of these HOFs as robust hydrophobic adsorbents for engineering purposes. Beyond mitigating surface polarity, achieving optimal C_2H_6 recognition demands a precisely tailored pore geometry. Herein lies a critical limitation of HOFs assembled primarily through π–π stacking.[42–45] The intrinsic cofacial geometry of this interaction hinders the effective projection of the π-electron cloud onto the pore interior, creating a spatially incongruous environment for C_2H_6. As a result, the pore walls are deficient in contact points precisely oriented along the molecular axis of C_2H_6, which severely curtails the van der Waals forces and thus limits the ultimate binding affinity. A conceptually new strategy to circumvent this limitation is to spatially lock the aromatic cores *via* programmable hydrogen-bonding arms, thereby creating tailored pore chemistry, yet it has never been realized in carboxylic acid-based HOFs.

Dislocation pinning is a cornerstone strengthening mechanism in metallurgy, in which microstructural obstacles immobilize dislocations and thereby suppress plastic deformation.[46,47] By anchoring these line defects, pinning sites impede their glide under stress, necessitating a substantially higher energy input for their movement. This powerful concept of frustrating periodic arrangements *via* engineered obstacles can be translated into molecular design. Specifically, introducing localized steric hindrances within molecular precursors can act as "molecular pins" to disrupt periodic π–π stacking, enabling rational control over the resulting supramolecular configuration (Scheme 1).

Inspired by this concept, we present a spatial pinning strategy for HOFs to force the rotation of hydrogen-bonding arms by pinning molecular struts in the precursor. Herein, we report an exceptional inert HOF, designated **HOF-ZSTU-5** (ZSTU represents Zhejiang Sci-Tech University). The deliberate installation of methyl groups imparts pronounced steric repulsion between the hydrogen-bonding arms and the aromatic core, forming a stereoscopic precursor conformation. Consequently, the assembled HOF eliminates π–π stacking and establishes a distinctive four-way interconnected cavity within the interlayer voids. The pyrene core is fully oriented toward the pore walls, significantly enhancing the inertness of the framework. Notably, the carboxylic acid hydrogen-bonded dimer is embedded within the framework rather than exposed at the pore surface, realizing global inertness in carboxylic acid-based HOFs, as evidenced by a water contact angle of up to 153° and a saturated water adsorption capacity of only 0.057 g g^{-1} at room temperature. Gas sorption isotherms reveal that the inert environment enables high C_2H_6 adsorption capacity (91.5 cm^3 g^{-1}) and packing density (0.349 kg L^{-1}), achieving a C_2H_6/C_2H_4 selectivity of 2.0. Gas-loaded single crystals and theoretical calculations reveal that the optimal binding configuration of C_2H_6 within the cavities yields a high adsorption enthalpy while minimizing van der Waals forces with C_2H_4. Dynamic breakthrough tests further validate that **HOF-ZSTU-5** can achieve high-purity C_2H_4 (>99.9%) in one step from mixed gases with varying flow rates and ratios, with a productivity of up to 36.0 L kg^{-1}. Remarkably, this high-performance separation is robust against humidity, highlighting the potential of **HOF-ZSTU-5** for efficient C_2H_4 purification.

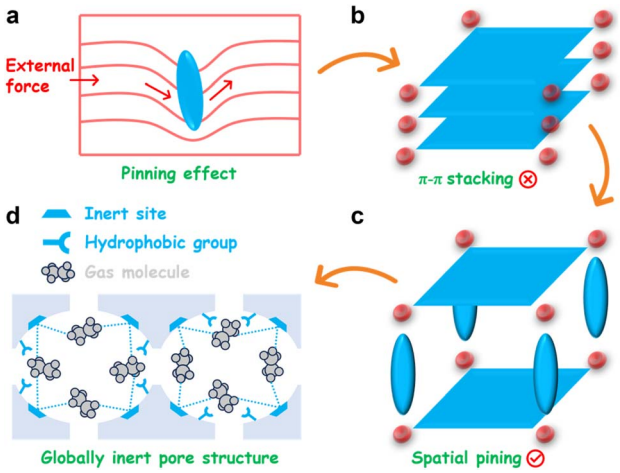

Scheme 1 Spatial pinning strategy for an overall hydrophobic HOF for preferential adsorption of C_2H_6. (a) Illustration of dislocation pinning. (b) Elimination of π–π stacking by (c) molecular pins separating adjacent layers to generate pore space. (d) Globally inert pore structure produced by this strategy, featuring pyrene cores fully oriented toward the pore surface and methyl sites.

Results and discussion

Synthesis, structure, and characterization

The light yellow-green rhombic crystals of **HOF-ZSTU-5** were obtained by diffusing *n*-hexane or cyclohexane into a methanol (MeOH) solution of 4,4′,4″,4‴-(pyrene-1,3,6,8-tetrayl)tetrakis(3-methylbenzoic acid) (TBAPy-3-CH_3) at room temperature (Fig. 1a). Single crystal X-ray diffraction (SCXRD) analysis

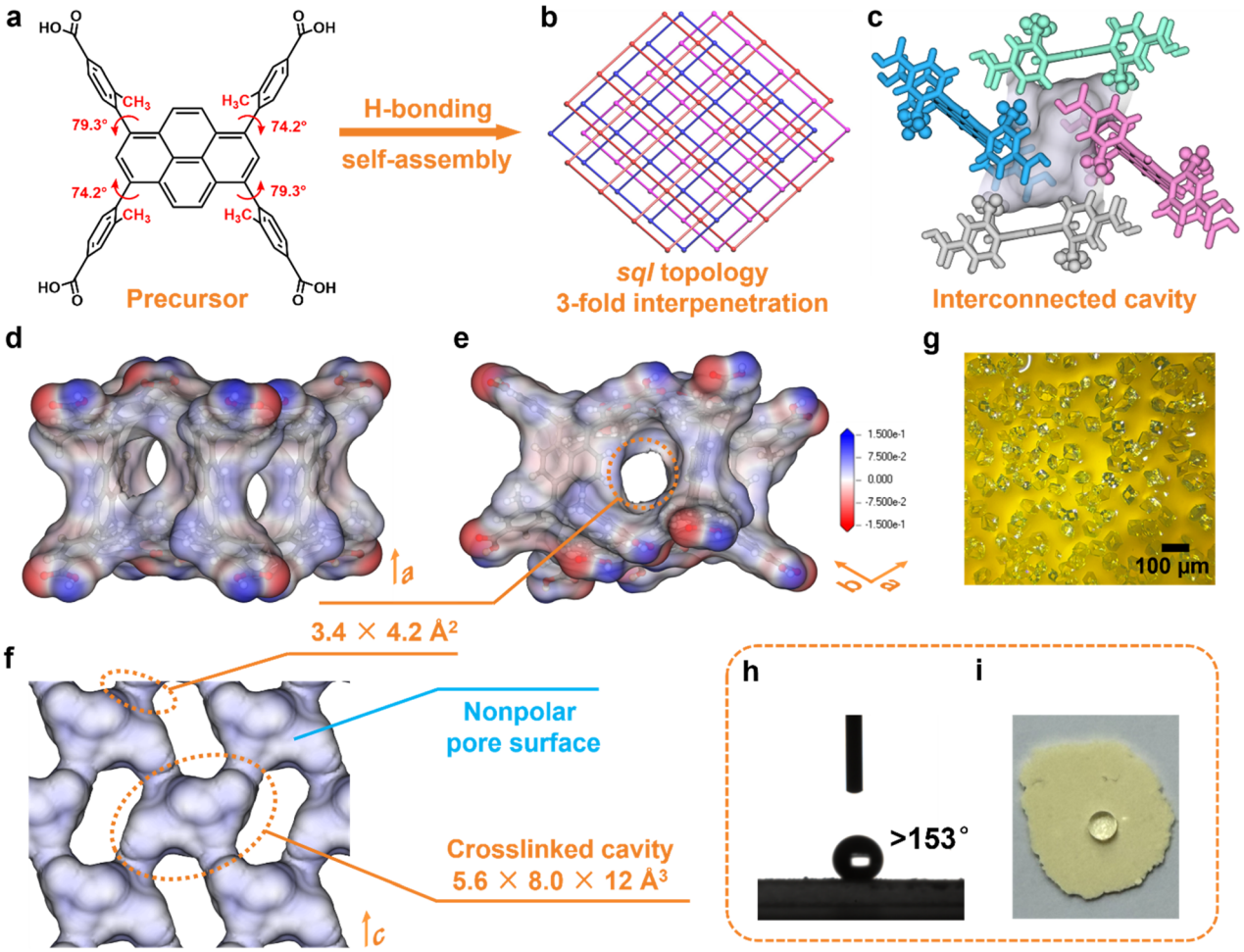

Fig. 1 Structure and properties of **HOF-ZSTU-5**. (a) Conformation of the TBAPy-3-CH_3 precursor, showing two dihedral angles between the carboxyphenyl and pyrene core; (b) the *sql* topology with 3-fold interpenetration; (c) the four-way interconnected cavities established by interlayer interpenetration; (d)–(f) electrostatic potential mapped onto the pore surface of **HOF-ZSTU-5**, with pore dimensions indicated. Blue and red colors represent positive and negative potentials, respectively; (g) an optical micrograph of a typical as-synthesized crystal; (h) water contact angle measurement and contact angle of **HOF-ZSTU-5**; and (i) snapshot of a water droplet on the sample surface.

revealed that **HOF-ZSTU-5** crystallizes in the orthorhombic space group *Pbca* (Table S1). The asymmetric unit of **HOF-ZSTU-5** contains one half of a TBAPy-3-CH_3 molecule, which is symmetric about the para-axis of the carboxyphenyl arm. Each precursor forms four hydrogen-bonding units, consisting of carboxyl···carboxyl hydrogen-bonded dimers with O···O distances of 2.651 and 2.725 Å, which extend into a two-dimensional (2D) hydrogen-bonded network (Fig. S1). In the TBAPy-3-CH_3 precursor, strong steric hindrance arises between the pyrene core and the carboxyphenyl group due to methyl pinning, resulting in high dihedral angles of 74.2 and 79.3° (Fig. S2), which eliminates π–π stacking induced by the proximity of π-conjugated planes. By comparison, the dihedral angle in the parent **HOF-101** (also known as **PFC-1**)[48,49] precursor is only 37.9°. This highly twisted steric configuration of TBAPy-3-CH_3 enhances the stability of the framework through the formation of C–H···O hydrogen bonds and multiple van der Waals interactions (Fig. S3). Each hydrogen-bonded layer of **HOF-ZSTU-5** entangles with two other layers at a planar angle of 48.4°, forming a 3-fold interpenetrated *sql* framework (Fig. 1b and S1). Within this three-dimensional (3D) framework, an interconnected cavity with dimensions of 5.6 × 8.0 × 12 $Å^3$ is defined between the interpenetrating layers, which is surrounded by four TBAPy-3-CH_3 from different layers (Fig. 1c). Among these, the pyrene cores of one pair of parallel TBAPy-3-CH_3 are oriented toward the cavity, lining its surface with an inert environment. The other two TBAPy-3-CH_3 delimit four pore windows of 3.4 × 4.2 $Å^2$ that connect the adjacent cavities (Fig. 1d, e and S4). Each pore window is gated by two methyl groups, which serve dual functions as spatial confinement agents and binding sites. Importantly, the interlayer interpenetration strategically shields the polar carboxylic acid dimers within the framework and away from the pore region. The resulting inert pore environment, which is confirmed by electrostatic potential mapping of the cavities, significantly enhances the binding affinity for nonpolar gas molecules (Fig. 1f, S5 and S6).

The phase purity of **HOF-ZSTU-5** was verified by powder X-ray diffraction (PXRD) analysis, with the experimental patterns for both the as-synthesized and activated samples showing

excellent agreement with the pattern simulated from single crystal diffraction data (Fig. S7). The high structural order is visualized by optical microscopy (OM) and scanning electron microscopy (SEM), which show uniformly shaped crystals whose morphology is predicted using the Bravais–Friedel–Donnay–Harker (BFDH) algorithm for thermodynamically stable growth (Fig. 1g, S8 and S9). Thermogravimetric analysis (TGA) of the activated **HOF-ZSTU-5** (denoted **HOF-ZSTU-5a**) revealed a thermal decomposition onset above 340 °C under a N_2 atmosphere (Fig. S10). This superior thermal stability, which surpasses that of the parent framework, can be attributed to the robust interpenetrated architecture stabilized by the pinned, rigid conformation.

Contact angle and water sorption experiments

Water contact angle tests were conducted on a series of carboxylic acid-based HOFs to assess their apparent hydrophobicity (Fig. 2 and S11–S14). The infiltration of water droplets was observed on the surfaces of the other eight activated carboxylic acid-based HOFs, although the time required for complete infiltration varied among these HOFs. In contrast, only gravitational deformation without discernible spreading was observed on the surface of **HOF-ZSTU-5a**. Five consecutive contact angle measurements confirmed that **HOF-ZSTU-5a** exhibited a water contact angle of at least 153°, demonstrating superhydrophobicity (Fig. S15). This finding confirms our hypothesis that the spatial pinning strategy, which structurally buries the polar hydrogen-bonding networks, is highly effective in minimizing surface wettability. The superhydrophobicity of **HOF-ZSTU-5a** is remarkable, exceeding not only typical carboxylic acid-based HOFs but also prominent non-carboxylic examples such as **HOF-FJU-1a** (141°, Fig. S16),[50] **MTHOF-1** (121.4°),[51] and **HOF-NKU-1** (87.8°),[42] as well as other classes of porous materials (Table S4).

To probe the intrinsic hydrophobicity of the pore interior, water vapor sorption isotherms of carboxylic acid-based HOFs were measured at 298 K (Fig. 3b and S17–S21). The water uptake of **HOF-ZSTU-5a** at near saturation is only 0.057 g g^{-1}, which is 1/13 and 1/10 of that of **HOF-101** (0.773 g g^{-1}) and **HOF-101-CH_3** (0.577 g g^{-1}),[52] respectively, and comparable to that of **ZJU-HOF-5a** (0.059 g g^{-1}).[53] Even when compared to other carboxylic acid-based HOFs and C_2H_6-selective adsorbents, it remains at a low value (Fig. 3c and Table S5). Combined with its superhydrophobic surface, **HOF-ZSTU-5a** represents a rare example of an overall hydrophobic material, similar to but superior to **SMS-POC-1**.[54] This is a rare attribute for hydrogen-bonded architectures, implying that the spatial pinning strategy effectively prevents water clustering within the pores, thereby paving the way for robust separation performance in humid environments.

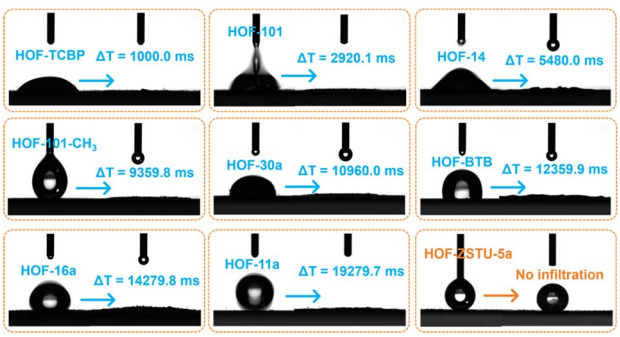

Fig. 2 Snapshots of contact angle measurements for a series of carboxylic acid-based HOFs, showing the time required for water droplets to fully infiltrate from the moment of contact with the HOF surface. Among them, HOF-ZSTU-5a exhibits no infiltration due to its superhydrophobicity.

Porosity and C_2 gas uptake measurements

The potential porosity of **HOF-ZSTU-5a** was calculated to be 33.4% using the PLATON solvent model.[55] The pore volume calculated from the crystal structure is 0.358 cm^3 g^{-1}. The experimental permanent porosity was determined from the N_2 sorption isotherm at 77 K (Fig. 3a and S22). **HOF-ZSTU-5a** exhibits a typical type I microporous isotherm, with a total N_2 uptake of 314 cm^3 g^{-1}, corresponding to a Brunauer–Emmett–Teller (BET) surface area of 1060 cm^2 g^{-1} (Fig. S23). The DFT pore size model revealed that the apertures of **HOF-ZSTU-5a** are concentrated at 5.9, 8.0, and 11.8 Å, which fits well with the dimensions of the interconnected cavity. This relatively shrunken nonpolar pore structure is expected to enhance the binding affinity to the target gas and facilitate dense packing.

Single-component sorption isotherms were used to evaluate the actual effect of different pore structures on gas sorption capacity. At 298 K and 1 bar, **HOF-ZSTU-5a** exhibits a remarkably high C_2H_6 uptake of 91.5 cm^3 g^{-1} and a C_2H_4 uptake of 78.2 cm^3 g^{-1} (Fig. 3d). This performance significantly surpasses that of the parent **HOF-101** (61.7 and 52.0 cm^3 g^{-1} of C_2H_6 and C_2H_4 respectively) and **HOF-101-CH_3** (37.6 and 25.9 cm^3 g^{-1}). The superior capacity of **HOF-ZSTU-5a** highlights the advantage of the spatial pinning strategy: the resulting tighter pore confinement enhances van der Waals contacts, whereas the larger, open pores of the reference frameworks fail to interact strongly with the gas molecules. At 273 K, the uptake of **HOF-ZSTU-5a** for C_2H_6 and C_2H_4 further increases to 110.0 and 98.9 cm^3 g^{-1} (Fig. S24). Notably, the C_2H_6 capacity of **HOF-ZSTU-5a** at 298 K ranks among the top tier of reported HOFs, second only to **ZJU-HOF-1** (109 cm^3 g^{-1}),[39] and outperforms a range of prominent HOFs including **HOF-NBDA** (89.2 cm^3 g^{-1}),[41] **HOF-76a** (66.1 cm^3 g^{-1}),[56] and **NKPOC-DS** (61.6 cm^3 g^{-1}),[57] as well as benchmark MOFs such as **$Fe_2(O_2)$(dobdc)** (74.3 cm^3 g^{-1}),[9] **$Cu(Qc)_2$** (41.5 cm^3 g^{-1}),[58] and **PCP-IPA** (41.5 cm^3 g^{-1}).[59] To quantify the filling efficiency, the C_2H_6 packing density in **HOF-ZSTU-5a** was determined to be 0.349 kg L^{-1}, which is 286 times that of gaseous C_2H_6 under identical conditions (1.22×10^{-3} kg L^{-1}), underscoring its exceptional pore-filling efficiency (Fig. 3e).

The isosteric heat of adsorption (Q_{st}) was derived from the isotherms at 298 and 273 K using the Virial equation (Fig. S25–S28). At zero coverage, **HOF-ZSTU-5a** exhibits a Q_{st} of 32.9 kJ mol^{-1}. This value falls within the ideal range for physisorption, indicating that the nonpolar pore walls provide adequate van der Waals attraction for efficient capture, while

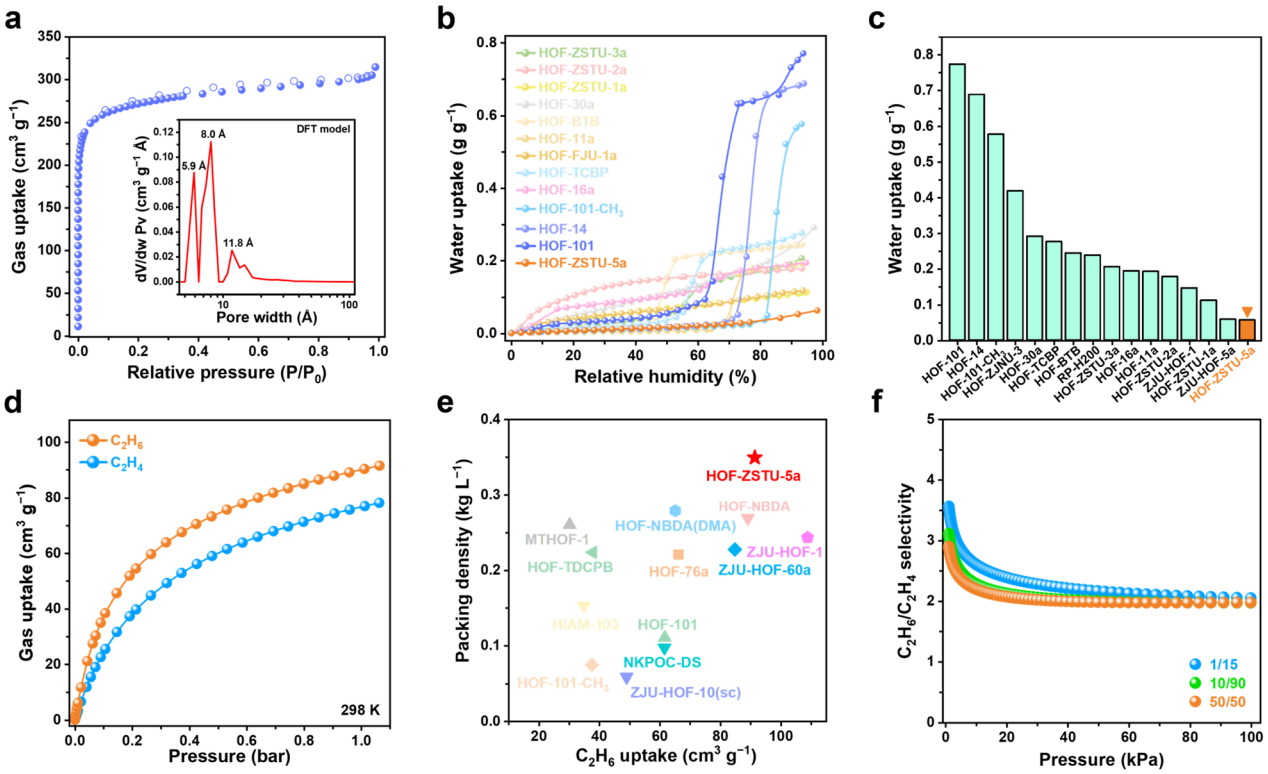

Fig. 3 (a) The 77 K N_2 sorption isotherm of **HOF-ZSTU-5a** and its pore size distribution. (b) Water uptake isotherms of a series of carboxylic acid-based HOFs at 298 K. (c) Water uptake of carboxylic acid-based HOFs at 298 K and near-saturation humidity. (d) Single-component gas sorption isotherms of **HOF-ZSTU-5a** at 298 K. (e) The uptake and packing density of C_2H_6 for C_2H_6-selective HOFs were comprehensively compared. (f) C_2H_6/C_2H_4 selectivity of **HOF-ZSTU-5a** at 298 K.

avoiding the excessive energy penalties associated with difficult regeneration. Dynamically, the Q_{st} curve initially declines as preferred binding sites are saturated, but subsequently rises at higher loadings. This inflection signifies the onset of strong cooperative guest–guest interactions, providing thermodynamic evidence for the dense packing mechanism within the confined pores. Ultimately, by achieving a synergy of high capacity, exceptional packing density, and energy-efficient binding (Q_{st}), **HOF-ZSTU-5a** sets a new performance standard among C_2H_6-selective porous materials (Fig. S29 and Tables S6, S7).

To evaluate the separation efficiency for binary mixtures, selectivities were calculated based on Ideal Adsorbed Solution Theory (IAST) (Fig. S30–S32). **HOF-ZSTU-5a** maintained the highest selectivity across the entire pressure range, with a selectivity of 2.0 at 1 bar, representing a marked improvement over **HOF-101-CH$_3$** (1.45) and **HOF-101** (1.3) (Fig. 3f). Even for a typical low-concentration cracked gas mixture (v/v = 1/15, C_2H_6/C_2H_4), **HOF-ZSTU-5a** exhibits a high selectivity of 2.05 (Fig. S33). Furthermore, the separation potential (Δq) was used as a combined indicator to weigh the trade-off between the capacity and selectivity of adsorbents (Fig. S34 and S35). Remarkably, the Δq value of **HOF-ZSTU-5a** (1.22 mmol g^{-1}) was superior to that of **HOF-101-CH$_3$** (0.25 mmol g^{-1}), **HOF-101** (0.31 mmol g^{-1}), **MTHOF-1** (0.51 mmol g^{-1}), and **HOF-76a** (0.81 mmol g^{-1}), as well as many C_2H_6-selective MOFs (Table S8). These results confirm that the spatial pinning configuration successfully creates a stereochemical environment that is optimally tuned for C_2H_6, simultaneously maximizing uptake and selectivity to achieve superior separation performance.

GCMC simulation study

The binding behavior between guest molecules and the host framework was investigated using grand canonical Monte Carlo (GCMC) simulations. At 298 K and 100 kPa, the simulations for **HOF-ZSTU-5a** identified three high-density regions for C_2H_6 at the cavity wall (site I) and center (site II), whereas C_2H_4 presented only two symmetrical distributions, corresponding to a saturation loading of three C_2H_6 or two C_2H_4 molecules per unit cavity (Fig. S36 and S37). These guest molecules exhibit anisotropic distribution, favoring the longer pathway between opposing cavity openings rather than uniform distribution across all four openings. This directional preference arises from favorable molecular diffusion kinetics, possibly driven by energy barriers or steric constraints. In contrast, both homologous HOFs based on π–π stacking exhibit a marked underfilling of the guests (Fig. S38–S41), implying that larger pore sizes and heterogeneous pore polarity is detrimental to the formation of affinity sites. Due to the presence of *ortho*-methyl groups, the guest approaches the pyrene sidewalls of the **HOF-101-CH$_3$** pore in a co-planar orientation, whereas in **HOF-101** without methyl group sites, it is in a perpendicular orientation.

This suggests that guest molecules are adaptively captured in the framework according to the pore structural properties. Overall, the combination of a homogeneous, globally inert cavity surface and an optimized diffusive pore topology represents a key advantage of **HOF-ZSTU-5a** for maximizing pore utilization.

Gas-loaded single crystal configuration

The crystal structures of **HOF-ZSTU-5a** loaded C_2H_6 or C_2H_4 were determined by *in situ* SCXRD (Fig. S42 and Tables S2, S3). The gas-loaded single crystals (**C_2H_4@HOF-ZSTU-5a** at 273 K and **C_2H_6@HOF-ZSTU-5a** at 273 K) reveal two symmetrically distributed molecules of C_2H_6 or C_2H_4 per cavity (Fig. S43). The gas-loaded conformation of C_2H_4 is consistent with theoretical simulations, while only an incomplete symmetric distribution form of C_2H_6 in the cavity is observed. The lack of central C_2H_6 implies unresolved kinetic or thermodynamic factors, which motivates us to investigate the interactions and adsorption kinetics of guests in the pores at low temperatures. Two crystallographically independent C_2H_6 molecules were identified using a C_2H_6-loaded **HOF-ZSTU-5a** crystal at 150 K (**C_2H_6@HOF-ZSTU-5a** at 150 K), forming guest–guest interactions with three short-range orientational forces at distances of 2.355–2.947 Å for dense packing in the pore (Fig. 4a and b). The two C_2H_6 occupy distinct adsorption sites at the cavity edge and center, consistent with theoretical calculations (Fig. S44 and S45). The C_2H_6 at site I was close to the cavity wall consisting of two TBAPy-3-CH_3, forming three moderately strong C–H···π hydrogen bonds (2.718–2.926 Å) with one pyrene core, and a C–H···C van der Waals dispersion force (3.214 Å) with the other precursor. In addition, it is subject to four C–H···C induced dipole interactions from two *meta*-methyl groups, with lengths of 2.680–3.246 Å (Fig. 4c). Such spatial confinement arises from the enthalpic trap that C_2H_6 needs to overcome when passing through cavity apertures narrower than their kinetic diameter. For the C_2H_6 at site II (Fig. S46), only two sets of C–H···C van der Waals interactions (3.479 and 3.494 Å) with the two symmetric precursors were observed, indicating weakened host–guest interaction in the central region. This weak binding tends to be hidden by molecular thermal motions with increasing temperature, explaining the inability of C_2H_6 from site II to be resolved at ambient temperature. The C_2H_4-loaded single crystals (**C_2H_4@HOF-ZSTU-5a** at 150 K) show only one crystallographically symmetric distribution of C_2H_4 in the cavity (Fig. 4e). Owing to its larger quadrupole moment (Table S9), C_2H_4 preferentially resides in regions of enhanced polarity. As a result, the two symmetric C_2H_4 molecules are positioned closer to the cavity center, exhibiting guest–guest interactions with lengths of 3.433–3.717 Å (Fig. 4f), which are longer than the interactions between C_2H_6 molecules. The C_2H_4 forms two C–H···π hydrogen bonds (3.162 and 3.390 Å) with the pyrene core and two C–H···C van der Waals dispersion interactions (3.318 and 3.692 Å) with aromatic rings, and two C–H···C interactions (3.166 and 3.443 Å) with two *meta*-methyl groups (Fig. 4g). The weak host–guest interactions indicate a low compatibility of C_2H_4 with the inert pore environment. A comparison of the four gas-loaded single crystals revealed a moderate lattice expansion in C_2H_6-loaded crystals at ambient temperature (+0.9%)

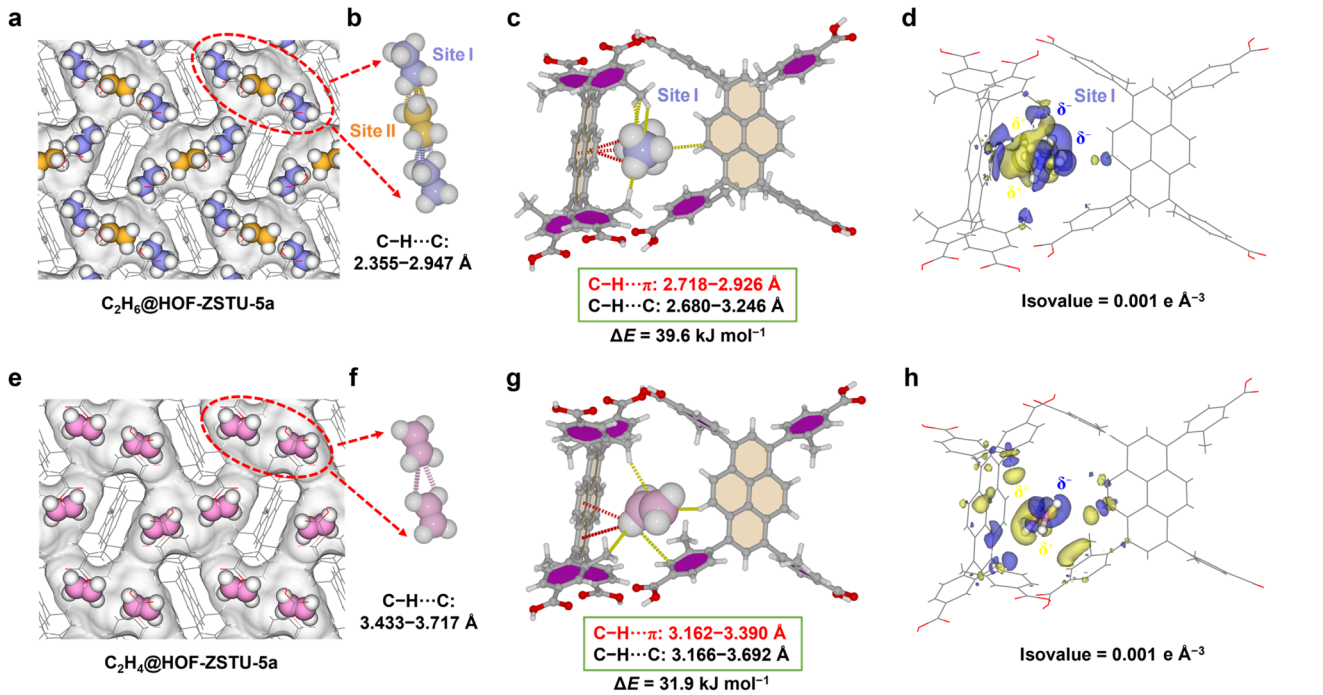

Fig. 4 HOF-ZSTU-5a crystal structure of *in situ* loaded (a) C_2H_6 and (e) C_2H_4 at 150 K. The guest–guest interactions between (b) three C_2H_6 and (f) two C_2H_4 molecules in a single cavity. The host–guest interaction forms between the framework and (c) site I C_2H_6, and (g) C_2H_4 in the gas-loaded single crystal. Differential electron density map between the framework and (d) site I C_2H_6, and (h) C_2H_4, where the blue region denotes charge aggregation and the yellow region denotes charge dissipation.

compared to those at low temperature, whereas C_2H_4-loaded crystals exhibited only a slight expansion (+0.2%). The differential expansion phenomenon is related to the occupancy of the guest molecules and the host–guest interactions, which suggests a thermodynamically driven framework adaptive effect. The above results show a dual distribution of C_2H_4 in the cavity without additional adsorption sites. This binding behavior is attributed to the incompatibility between the π-electrons from the C_2H_4 C=C bond and the nonpolar pore environment, blocking C_2H_4 from occupying the "sweet spot" of site binding and thereby reducing uptake.

The host–guest energies of the optimized gas-loaded single crystals were calculated using first-principles dispersion-corrected density functional theory (DFT-D). The static binding energies of C_2H_6 at the edge and center of the cavity are 39.6 and 29.7 kJ mol^{-1}. The calculated weighted average of 36.3 kJ mol^{-1} is notably higher than that of C_2H_4 (31.9 kJ mol^{-1}). These values align well with the Q_{st} at zero coverage, confirming that guest molecules exhibit enhanced binding affinity near the pore walls. The preferential binding sites for C_2H_6/C_2H_4 in the other two HOFs are located on the pyrene sidewalls, with binding energies of 30.5/24.2 kJ mol^{-1} to **HOF-101** and 20.4/18.4 kJ mol^{-1} to **HOF-101-CH$_3$** (Fig. S47 and S48). This comparative result indicates that while the pores of **HOF-101** permit effective interaction with the pyrene surface, the steric bulk of the *ortho*-methyl groups in **HOF-101-CH$_3$** displaces the guest molecules away from the π-surfaces. This increased separation distance drastically diminishes the dominant dispersion forces, which cannot be sufficiently compensated for by the methyl–guest interactions, resulting in the lowest binding affinity.

The variations of the charge distributions of the guest and the framework were further calculated. For the gas-loaded single crystal of **HOF-ZSTU-5a** at 150 K, C_2H_6 exhibits a stronger charge shift than C_2H_4 at the same isovalue (Fig. 4d). In particular, the methyl group electron cloud of C_2H_6 at site I shifts toward the pyrene core and the *meta*-methyl group. This rearrangement facilitates a $C^{\delta-}_{(ethane)}$–$H^{\delta+}_{(ethane)}\cdots C^{\delta-}_{(framework)}$ dispersion interaction. Concurrently, the carboxyphenyl groups shift electron density toward the C_2H_6, reinforcing the $C^{\delta-}_{(framework)}$–$H^{\delta+}_{(framework)}\cdots C^{\delta-}_{(ethane)}$ interaction. The charge shift of the central C_2H_6 is relatively weak and relevant to its lower binding energy (Fig. S46). A noticeable electron rearrangement also occurs as the π-electron of C_2H_4 shifts toward the aromatic rings and pyrene core (Fig. 4h), although to a lesser extent than in C_2H_6. We also describe the host–guest contact distances by mapping the d_{norm} values onto the Hirshfeld surface of the guest molecules to quantify these interactions.[60] The contact distance becomes shorter than the sum of the van der Waals radii when d_{norm} is negative, which is shown in red, indicating a strong intermolecular interaction. In **HOF-ZSTU-5a**, the strong contact of C_2H_6 exists not only with the pyrene core and *meta*-methyl group, but also between the C_2H_6 molecules, with the minimum d_{norm} values of −0.5717 and −0.4870 for site I and site II (Fig. S49). A much weaker contact for C_2H_4 is evident, with a minimum d_{norm} value of 0.2095 (Fig. S50). The types of interactions between the guest molecules and the framework were analyzed through 2D fingerprint plots. The short-range and concentrated distances of C_2H_6 (0.6–2.3 Å) and the framework (0.8–2.9 Å) on the Hirshfeld surface are composed of 79.7% H···H and 20.3% H···C, embodied in C–H···π and C–H···C interactions (Fig. S49). The distance between C_2H_4 and the framework on the Hirshfeld surface is longer and more dispersed, with 77.9% H···H and 19.5% H···C, and the remaining 2.6% C···C reflecting repulsion between the $C^{\delta-}_{(ethylene)}$ and $C^{\delta-}_{(framework)}$ (Fig. S50). The above discussion strongly confirms that a globally inert pore environment not only provides multiple interactions for C_2H_6, but also creates suitable steric confinement, which is essential for achieving preferential adsorption of C_2H_6 over C_2H_4.

Dynamic breakthrough experiments

Considering the selective compatibility of the interconnected cavity with C_2H_6, the dynamic separation performance of **HOF-ZSTU-5a** for C_2H_6/C_2H_4 mixed gases under different conditions was evaluated from a practical application perspective. First, dynamic breakthrough experiments were conducted at 298 K using equimolar C_2H_6/C_2H_4 mixtures at low total flow rates of 1 and 2 mL min^{-1} (Fig. 5a and S51). As the binary gas mixture passes through the fixed bed packed with the activated adsorbent, polymer-grade C_2H_4 (99.9%) is initially detected at the outlet. Once the adsorbent reaches dynamic saturation, the C_2H_4 outflow concentration begins to decrease, at which point C_2H_6 breaks through from the fixed bed. After calibration by adsorbent mass, the retention times of C_2H_4 at the two flow rates were 27.3 and 17.1 min g^{-1}. Breakthrough curve calculations for **HOF-ZSTU-5a** yield C_2H_4 productivities of 12.2 and 13.3 L kg^{-1} for purities >99.9% in one cycle. The good separation performance was maintained even when half the adsorbent mass is used (Fig. S51). To optimize the process space-time yield and suppress mass-transfer zone tailing, the flow rate was elevated to 4 mL min^{-1} under the same conditions (Fig. 5b). The C_2H_4 yield per cycle reached 17.5 L kg^{-1}, comparable to that of **Fe$_2$(O$_2$)(dobdc)** (17.7 L kg^{-1}), while the total dynamic separation time was reduced to approximately 60 min g^{-1}, optimizing the balance between production efficiency and separation performance. Moreover, using a 10/90 (v/v) C_2H_6/C_2H_4 mixture to simulate industrial feed conditions yielded a C_2H_4 productivity of 36.0 L kg^{-1} (Fig. 5c), which is more than twice that of an equimolar mixture and comparable to that of **SNNU-181-Mn$_{3+6}$** (39.6 L kg^{-1}) as a benchmark material.[61] The specific injection amount of the gas mixture was used as a normalized indicator of the breakthrough flow rate and runtime to evaluate various HOFs and MOFs.[62] In equimolar mixtures, **HOF-ZSTU-5a** showed the optimal balance among HOFs with the highest specific injection amount (2.14 mmol g^{-1}), which was 1.6 times higher than the second-ranked **HOF-NBDA** and **NKPOC-DS** (1.38 mmol g^{-1}) (Fig. 5d and Table S6) and also higher than MOF materials such as **Fe$_2$(O$_2$)(dobdc)** (1.99 mmol g^{-1}), **Zn-atz-ipa** (0.5 mmol g^{-1}),[63] and **PCP-IPA** (1.41 mmol g^{-1}), second only to **TYUT-17** (3.13 mmol g^{-1}) (Fig. S52 and Table S10).[64] We also performed breakthrough tests on **HOF-101** and **HOF-101-CH$_3$** at room temperature (Fig. S53 and S54). For 10/90 (v/v) mixtures,

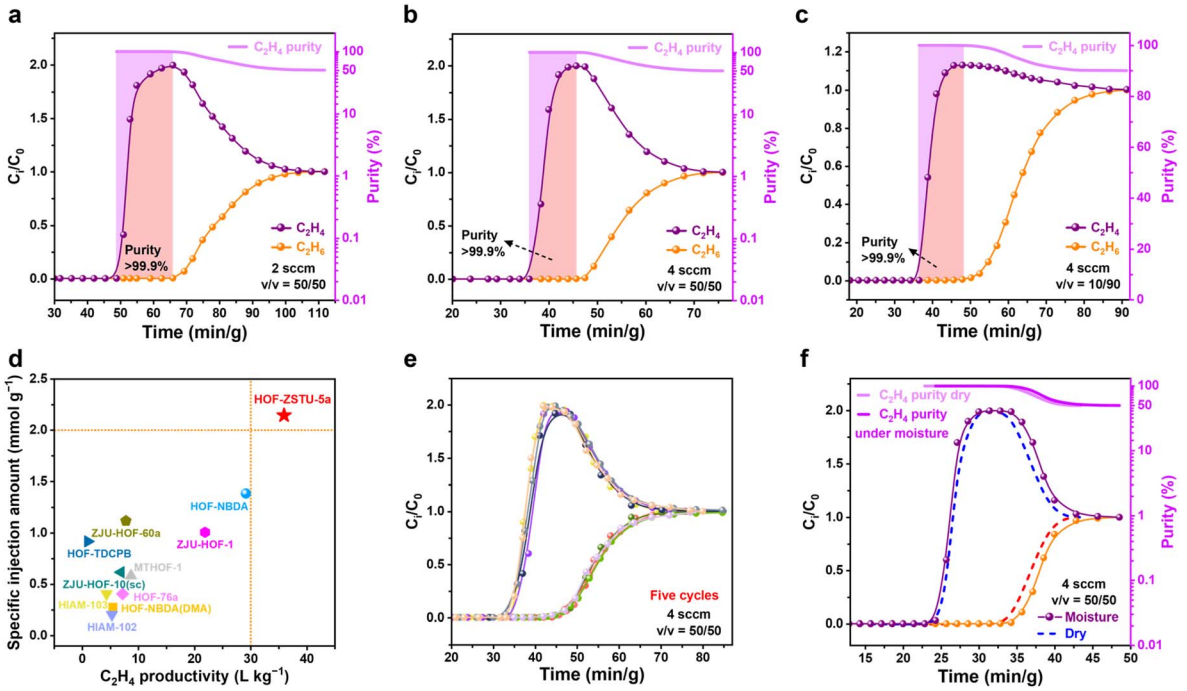

Fig. 5 The breakthrough tests of **HOF-ZSTU-5a** were performed at 298 K and 1 bar for equimolar C_2H_6/C_2H_4 mixtures with flow rates of (a) 2 mL min^{-1} and (b) 4 mL min^{-1} and (c) C_2H_6/C_2H_4 of 10/90 (v/v) at a flow rate of 4 mL min^{-1}. (d) Comparison of the specific injection amount and C_2H_4 productivity of C_2H_6-selective HOFs. (e) Five consecutive breakthrough tests at 298 K. (f) Breakthrough test at near-saturation humidity and compared to dry conditions.

their penetration time intervals were 2.5 and 3.6 min g^{-1}. Despite the short intervals, C_2H_4 productivities of 2.8 and 1.14 L kg^{-1} (>99.9%) were also obtained, respectively. However, C_2H_6 penetrated quickly out of the beds in equimolar mixtures, with C_2H_4 purities reaching only 96.0%. These breakthrough results verified that **HOF-ZSTU-5a** with a unique pore structure was able to intercept C_2H_6 for the one-step efficient separation and purification of C_2H_4.

Stability and comprehensive performance

Given the harsh nature of industrial environments, the robustness and practical feasibility of **HOF-ZSTU-5a** were rigorously evaluated. The material exhibited exceptional cycling stability, maintaining its uptake capacity over five static sorption–desorption cycles at 298 K (Fig. S55). This stability translates to dynamic conditions, as evidenced by five consecutive breakthrough runs without performance loss (Fig. 5e). Notably, complete regeneration was achieved under mild conditions (argon purge at 50 °C), a temperature significantly lower than typical thermal regeneration requirements. This regeneration temperature is well within the typical range of 40–100 °C used for industrial processes like pressure swing adsorption (PSA), positioning **HOF-ZSTU-5a** within the low-energy window for industrial separations. The chemical durability of **HOF-ZSTU-5a** is particularly striking. The framework retained its crystallinity and porosity after week-long immersion in diverse organic solvents and aqueous solutions ranging from pH 1 to 12. Most impressively, it withstood exposure to 12 M HCl, exhibiting negligible structural degradation (Fig. 6a, b and S56). Thermal stability was also assessed by exposing the samples to air at different temperatures for at least one hour, and the PXRD curves showed that **HOF-ZSTU-5a** remained highly crystalline

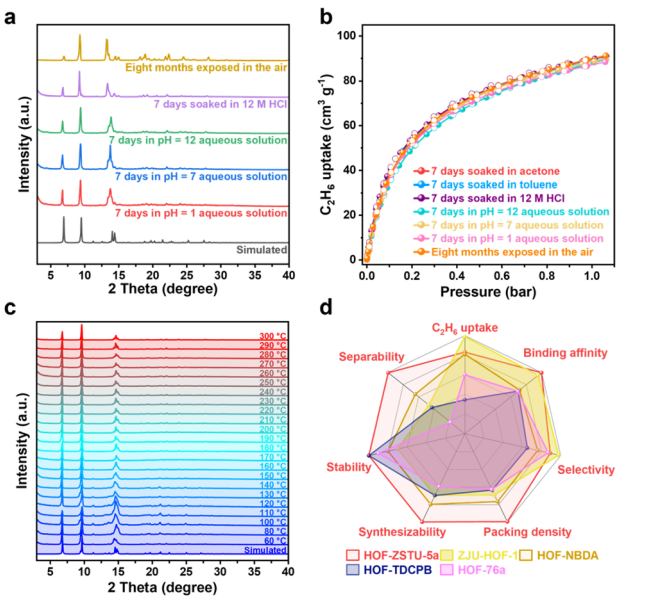

Fig. 6 (a) PXRD and (b) C_2H_6 sorption isotherms of **HOF-ZSTU-5a** after undergoing several different environmental stability experiments. (c) Variable-temperature PXRD curve of **HOF-ZSTU-5a**. (d) A comprehensive comparison of C_2H_6 uptake, binding affinity, selectivity, packing density, separability, stability, and synthesizability of **HOF-ZSTU-5a** and other high-performance carboxylic acid-based HOFs.

up to at least 300 °C (Fig. 6c). Notably, an enhanced breakthrough capacity was observed under near-saturated humidity, which is attributed to a weak synergistic effect between C_2H_6 and trace water molecules retained in the pore channels (Fig. 5f and S57).[65] Beyond performance, the material offers solution processability, a distinct advantage of HOFs. **HOF-ZSTU-5a** can be easily recrystallized from methanol, and the mother liquor is recyclable, underscoring its potential for sustainable, green manufacturing. Summarized by the radar chart comparing stability, capacity, selectivity, and productivity (Fig. 6d and Table S11), **HOF-ZSTU-5a** represents a holistic solution for robust and energy-efficient C_2H_4 purification.

Conclusions

In summary, we have engineered a distinct supramolecular conformation through a spatial pinning strategy. By strategically installing methyl groups to act as steric barriers, we successfully suppressed the conventional π–π stacking and assembled a robust HOF with a four-way interconnected pore structure. A multi-interpenetrating hydrogen-bonding network shields the polar carboxylic acid dimers, enabling the construction of a completely inert HOF. This defined pore structure enables a cooperative mechanism for C_2H_6/C_2H_4 separation: the pyrene core acts as the primary binding site for C_2H_6, while the methyl groups create constricted apertures that enhance selectivity through spatial confinement. The mechanism of preferential capture is rigorously validated by gas-loaded single crystals and DFT-D calculations. As a result, this HOF achieves the one-step production of high-purity C_2H_4 with a high productivity of 36.0 L kg^{-1} in dynamic breakthrough experiments. Its exceptional hydrophobicity ensures stable separation performance under humid conditions, underscoring industrial relevance. This study overcomes the intrinsic limitations of conventional π–π stacked HOFs through a target-oriented control of supramolecular conformation and further elucidates how the synergistic integration of functional sites and spatial strategies dictates the structure–property relationships in supramolecular frameworks.

Author contributions

Conceptualization: B. C., R.-B. L., J. G., and Y. C.; methodology and investigation: Y. C. and R. W.; single crystal analysis and refinement: J.-H. L., X. X., and Y. C.; writing—original draft: Y. C.; writing—review & editing: R.-B. L., J. G., and Y. C.; funding acquisition: B. C., R.-B. L., and J. G.

Conflicts of interest

The authors declare no competing interests.

Data availability

All other data supporting the findings of this study are included in the article and the supplementary information (SI) or are available from the lead contact upon reasonable request.

CCDC 2425853 (**HOF-ZSTU-5a**), 2425854 (**HOF-ZSTU-5**), 2425855 (**C_2H_4@HOF-ZSTU-5a** at 150 K), 2425856 (**C_2H_6@HOF-ZSTU-5a** at 150 K), 2425857 (**C_2H_4@HOF-ZSTU-5a** at 273 K) and 2425858 (**C_2H_6@HOF-ZSTU-5a** at 273 K) contain the supplementary crystallographic data for this paper.[66a-f]

Supplementary information: data collection and refinement details are listed in Tables S1–S3. See DOI: https://doi.org/10.1039/d5sc08507a.

Acknowledgements

This work was supported by the National Natural Science Foundation of China (No. 22378366, 22375221, and W2431013) and the Hundred Talents Program of Sun Yat-Sen University.

Notes and references

1 D. S. Sholl and R. P. Lively, Seven chemical separations to change the world, *Nature*, 2016, **532**, 435–437.
2 GlobalData, Ethylene Industry Capacity and Capital Expenditure Forecasts with Details of All Active and Planned Plants to 2028, https://www.globaldata.com/store/report/ethylene-market-analysis, accessed October 2025.
3 X. Wang, T. Zhao, J. Li, R. Wei, X. Xia and J. Gao, Programmed Pore Engineering in an Isoreticular Triazole–MOF Series for One-Step Ethylene Separation, *Angew. Chem., Int. Ed.*, 2025, e22675.
4 H. Wang, Y. Liu and J. Li, Designer metal–organic frameworks for size-exclusion-based hydrocarbon separations: progress and challenges, *Adv. Mater.*, 2020, **32**, 2002603.
5 Q. Ke, F. Xiong, G. Fang, J. Chen, X. Niu, P. Pan, G. Cui, H. Xing and H. Lu, The Reinforced Separation of Intractable Gas Mixtures by Using Porous Adsorbents, *Adv. Mater.*, 2024, **36**, 2408416.
6 S. Aguado, G. Bergeret, C. Daniel and D. Farrusseng, Absolute Molecular Sieve Separation of Ethylene/Ethane Mixtures with Silver Zeolite A, *J. Am. Chem. Soc.*, 2012, **134**, 14635–14637.
7 P. J. Bereciartua, Á. Cantín, A. Corma, J. L. Jordá, M. Palomino, F. Rey, S. Valencia, E. W. Corcoran, P. Kortunov, P. I. Ravikovitch, A. Burton, C. Yoon, Y. Wang, C. Paur, J. Guzman, A. R. Bishop and G. L. Casty, Control of zeolite framework flexibility and pore topology for separation of ethane and ethylene, *Science*, 2017, **358**, 1068–1071.
8 C. Gu, N. Hosono, J.-J. Zheng, Y. Sato, S. Kusaka, S. Sakaki and S. Kitagawa, Design and control of gas diffusion process in a nanoporous soft crystal, *Science*, 2019, **363**, 387–391.
9 L. Li, R.-B. Lin, R. Krishna, H. Li, S. Xiang, H. Wu, J. Li, W. Zhou and B. Chen, Ethane/ethylene separation in a metal-organic framework with iron-peroxo sites, *Science*, 2018, **362**, 443–446.
10 S. Du, J. Huang, M. R. Ryder, L. L. Daemen, C. Yang, H. Zhang, P. Yin, Y. Lai, J. Xiao, S. Dai and B. Chen, Probing sub-5 Ångstrom micropores in carbon for precise

light olefin/paraffin separation, *Nat. Commun.*, 2023, **14**, 1197.
11 Y. He, R. Krishna and B. Chen, Metal–organic frameworks with potential for energy-efficient adsorptive separation of light hydrocarbons, *Energy Environ. Sci.*, 2012, **5**, 9107–9120.
12 E. D. Bloch, W. L. Queen, R. Krishna, J. M. Zadrozny, C. M. Brown and J. R. Long, Hydrocarbon separations in a metal-organic framework with open iron(II) coordination sites, *Science*, 2012, **335**, 1606–1610.
13 C. Yu, Z. Guo, L. Yang, J. Cui, S. Chen, Y. Bo, X. Suo, Q. Gong, S. Zhang, X. Cui, S. He and H. Xing, A Robust Metal-Organic Framework with Scalable Synthesis and Optimal Adsorption and Desorption for Energy-Efficient Ethylene Purification, *Angew. Chem., Int. Ed.*, 2023, **62**, e202218027.
14 H. Zeng, X.-J. Xie, M. Xie, Y.-L. Huang, D. Luo, T. Wang, Y. Zhao, W. Lu and D. Li, Cage-Interconnected Metal–Organic Framework with Tailored Apertures for Efficient C_2H_6/C_2H_4 Separation under Humid Conditions, *J. Am. Chem. Soc.*, 2019, **141**, 20390–20396.
15 W. Liu, S. Geng, N. Li, S. Wang, S. Jia, F. Jin, T. Wang, K. A. Forrest, T. Pham, P. Cheng, Y. Chen, J.-G. Ma and Z. Zhang, Highly Robust Microporous Metal-Organic Frameworks for Efficient Ethylene Purification under Dry and Humid Conditions, *Angew. Chem., Int. Ed.*, 2023, **62**, e202217662.
16 Q. Ding, Z. Zhang, C. Yu, P. Zhang, J. Wang, X. Cui, C.-H. He, S. Deng and H. Xing, Exploiting equilibrium-kinetic synergetic effect for separation of ethylene and ethane in a microporous metal-organic framework, *Sci. Adv.*, 2020, **6**, eaaz4322.
17 N. C. Burtch, H. Jasuja and K. S. Walton, Water Stability and Adsorption in Metal–Organic Frameworks, *Chem. Rev.*, 2014, **114**, 10575–10612.
18 F. Chen, N. Prasetyo, S. Sakaki, K.-i. Otake and S. Kitagawa, Benchmark Paraffin Adsorption in a Super-Hydrophobic Porous Coordination Polymer with Blade-Like Circular Phenyl Nanotraps, *Angew. Chem., Int. Ed.*, 2025, **64**, e202423371.
19 H. Wang, B. Li, H. Wu, T.-L. Hu, Z. Yao, W. Zhou, S. Xiang and B. Chen, A Flexible Microporous Hydrogen-Bonded Organic Framework for Gas Sorption and Separation, *J. Am. Chem. Soc.*, 2015, **137**, 9963–9970.
20 R.-B. Lin and B. Chen, Hydrogen-bonded organic frameworks: chemistry and functions, *Chem*, 2022, **8**, 2114–2135.
21 W. Yang, A. Greenaway, X. Lin, R. Matsuda, A. J. Blake, C. Wilson, W. Lewis, P. Hubberstey, S. Kitagawa, N. R. Champness and M. Schröder, Exceptional Thermal Stability in a Supramolecular Organic Framework: Porosity and Gas Storage, *J. Am. Chem. Soc.*, 2010, **132**, 14457–14469.
22 Y. He, S. Xiang and B. Chen, A Microporous Hydrogen-Bonded Organic Framework for Highly Selective C_2H_2/C_2H_4 Separation at Ambient Temperature, *J. Am. Chem. Soc.*, 2011, **133**, 14570–14573.
23 X.-Z. Luo, X.-J. Jia, J.-H. Deng, J.-L. Zhong, H.-J. Liu, K.-J. Wang and D.-C. Zhong, A Microporous Hydrogen-Bonded Organic Framework: Exceptional Stability and Highly Selective Adsorption of Gas and Liquid, *J. Am. Chem. Soc.*, 2013, **135**, 11684–11687.
24 R. Zhang, H. Daglar, C. Tang, P. Li, L. Feng, H. Han, G. Wu, B. N. Limketkai, Y. Wu, S. Yang, A. X. Y. Chen, C. L. Stern, C. D. Malliakas, R. Q. Snurr and J. F. Stoddart, Balancing volumetric and gravimetric capacity for hydrogen in supramolecular crystals, *Nat. Chem.*, 2024, **16**, 1982–1988.
25 W. Wang, Y. Shi, W. Chai, K. W. K. Tang, I. Pyatnitskiy, Y. Xie, X. Liu, W. He, J. Jeong, J.-C. Hsieh, A. R. Lozano, B. Artman, X. Shi, N. Hoefer, B. Shrestha, N. B. Stern, W. Zhou, D. W. McComb, T. Porter, G. Henkelman, B. Chen and H. Wang, H-bonded organic frameworks as ultrasound-programmable delivery platform, *Nature*, 2025, **638**, 401–410.
26 I. Hisaki, C. Xin, K. Takahashi and T. Nakamura, Designing Hydrogen-Bonded Organic Frameworks (HOFs) with Permanent Porosity, *Angew. Chem., Int. Ed.*, 2019, **58**, 11160–11170.
27 F. Hu, C. Liu, M. Wu, J. Pang, F. Jiang, D. Yuan and M. Hong, An Ultrastable and Easily Regenerated Hydrogen-Bonded Organic Molecular Framework with Permanent Porosity, *Angew. Chem., Int. Ed.*, 2017, **56**, 2101–2104.
28 J. Gao, Y. Cai, X. Qian, P. Liu, H. Wu, W. Zhou, D.-X. Liu, L. Li, R.-B. Lin and B. Chen, A Microporous Hydrogen-Bonded Organic Framework for the Efficient Capture and Purification of Propylene, *Angew. Chem., Int. Ed.*, 2021, **60**, 20400–20406.
29 B. Yu, S. Geng, H. Wang, W. Zhou, Z. Zhang, B. Chen and J. Jiang, A Solid Transformation into Carboxyl Dimers Based on a Robust Hydrogen-Bonded Organic Framework for Propyne/Propylene Separation, *Angew. Chem., Int. Ed.*, 2021, **60**, 25942–25948.
30 X. Song, Y. Wang, C. Wang, X. Gao, Y. Zhou, B. Chen and P. Li, Self-Healing Hydrogen-Bonded Organic Frameworks for Low-Concentration Ammonia Capture, *J. Am. Chem. Soc.*, 2024, **146**, 627–634.
31 Y.-B. Wang, Y.-X. Lin, J.-X. Wang, X. Zhang, H. Wu, W. Zhou, B. Chen, G. Qian and B. Li, A Microporous Hydrogen-Bonded Organic Framework with Alkynyl Sites for Highly Efficient Propane/Propylene Separation, *J. Am. Chem. Soc.*, 2025, **147**, 24403–24412.
32 S. Lin, P. Ke, L. Wang, Y. Liang, J. Hu, L. Zhang, Z. Zhang, Y. He and B. Chen, Efficient Separation of Methanol-to-Olefins Products Using a Robust Polycatenated Hydrogen-Bonded Organic Framework, *Angew. Chem., Int. Ed.*, 2025, **64**, e202511773.
33 T. Takeda, M. Ozawa and T. Akutagawa, Jumping Crystal of a Hydrogen-Bonded Organic Framework Induced by the Collective Molecular Motion of a Twisted π System, *Angew. Chem., Int. Ed.*, 2019, **58**, 10345–10352.
34 T. Hashimoto, M. de la Hoz Tomás, R. Oketani, B. Cohen, M. Naruoka, N. Tohnai, A. Douhal and I. Hisaki, Single Crystalline, Non-Stoichiometric Hydrogen-Bonded Organic Frameworks Showing Versatile Fluorescence Depending on Composition Ratios and Distributions, *Angew. Chem., Int. Ed.*, 2025, **64**, e202419992.

35 B. Wang, R. He, L.-H. Xie, Z.-J. Lin, X. Zhang, J. Wang, H. Huang, Z. Zhang, K. S. Schanze, J. Zhang, S. Xiang and B. Chen, Microporous Hydrogen-Bonded Organic Framework for Highly Efficient Turn-Up Fluorescent Sensing of Aniline, *J. Am. Chem. Soc.*, 2020, **142**, 12478–12485.

36 P. Cui, E. Svensson Grape, P. R. Spackman, Y. Wu, R. Clowes, G. M. Day, A. K. Inge, M. A. Little and A. I. Cooper, An Expandable Hydrogen-Bonded Organic Framework Characterized by Three-Dimensional Electron Diffraction, *J. Am. Chem. Soc.*, 2020, **142**, 12743–12750.

37 I. Hisaki, Y. Suzuki, E. Gomez, Q. Ji, N. Tohnai, T. Nakamura and A. Douhal, Acid Responsive Hydrogen-Bonded Organic Frameworks, *J. Am. Chem. Soc.*, 2019, **141**, 2111–2121.

38 J.-R. Li, R. J. Kuppler and H.-C. Zhou, Selective gas adsorption and separation in metal–organic frameworks, *Chem. Soc. Rev.*, 2009, **38**, 1477–1504.

39 X. Zhang, J.-X. Wang, L. Li, J. Pei, R. Krishna, H. Wu, W. Zhou, G. Qian, B. Chen and B. Li, A Rod-Packing Hydrogen-Bonded Organic Framework with Suitable Pore Confinement for Benchmark Ethane/Ethylene Separation, *Angew. Chem., Int. Ed.*, 2021, **60**, 10304–10310.

40 Z. Ji, Q. Li, Y. Zhou, R. Krishna, M. Hong and M. Wu, Synergistic C_2H_2 Binding Sites in Hydrogen-Bonded Supramolecular Framework for One-Step C_2H_4 Purification from Ternary C2 Mixture, *Angew. Chem., Int. Ed.*, 2024, **63**, e202411175.

41 Y. Zhou, C. Chen, R. Krishna, Z. Ji, D. Yuan and M. Wu, Tuning Pore Polarization to Boost Ethane/Ethylene Separation Performance in Hydrogen-Bonded Organic Frameworks, *Angew. Chem., Int. Ed.*, 2023, **62**, e202305041.

42 L. Li, X. Zhang, X. Lian, L. Zhang, Z. Zhang, X. Liu, T. He, B. Li, B. Chen and X.-H. Bu, Flue gas desulfurization and SO_2 recovery within a flexible hydrogen-bonded organic framework, *Nat. Chem.*, 2025, **17**, 727–733.

43 M. O'Shaughnessy, J. Glover, R. Hafizi, M. Barhi, R. Clowes, S. Y. Chong, S. P. Argent, G. M. Day and A. I. Cooper, Porous isoreticular non-metal organic frameworks, *Nature*, 2024, **630**, 102–108.

44 C. A. Halliwell, K. Jolley, K. Yendall, M. R. J. Elsegood, G. N. Parkinson and A. Fernandez, A Simple and Sequential Strategy for the Introduction of Complexity and Hierarchy in Hydrogen-Bonded Organic Framework (HOF) Crystals for Environmental Applications, *Angew. Chem., Int. Ed.*, 2024, **63**, e202404452.

45 J.-H. Deng, J. Luo, Y.-L. Mao, S. Lai, Y.-N. Gong, D.-C. Zhong and T.-B. Lu, π-π stacking interactions: non-negligible forces for stabilizing porous supramolecular frameworks, *Sci. Adv.*, 2020, **6**, eaax9976.

46 M. D. Uchic, D. M. Dimiduk, J. N. Florando and W. D. Nix, Sample Dimensions Influence Strength and Crystal Plasticity, *Science*, 2004, **305**, 986–989.

47 Y. M. Wang, T. Voisin, J. T. McKeown, J. Ye, N. P. Calta, Z. Li, Z. Zeng, Y. Zhang, W. Chen, T. T. Roehling, R. T. Ott, M. K. Santala, P. J. Depond, M. J. Matthews, A. V. Hamza and T. Zhu, Additively manufactured hierarchical stainless steels with high strength and ductility, *Nat. Mater.*, 2018, **17**, 63–71.

48 K. Ma, P. Li, J. H. Xin, Y. Chen, Z. Chen, S. Goswami, X. Liu, S. Kato, H. Chen, X. Zhang, J. Bai, M. C. Wasson, R. R. Maldonado, R. Q. Snurr and O. K. Farha, Ultrastable Mesoporous Hydrogen-Bonded Organic Framework-Based Fiber Composites toward Mustard Gas Detoxification, *Cell Rep. Phys. Sci.*, 2020, **1**, 100024.

49 Q. Yin, P. Zhao, R.-J. Sa, G.-C. Chen, J. Lü, T.-F. Liu and R. Cao, An Ultra-Robust and Crystalline Redeemable Hydrogen-Bonded Organic Framework for Synergistic Chemo-Photodynamic Therapy, *Angew. Chem., Int. Ed.*, 2018, **57**, 7691–7696.

50 Y. Yang, L. Li, R.-B. Lin, Y. Ye, Z. Yao, L. Yang, F. Xiang, S. Chen, Z. Zhang, S. Xiang and B. Chen, Ethylene/ethane separation in a stable hydrogen-bonded organic framework through a gating mechanism, *Nat. Chem.*, 2021, **13**, 933–939.

51 H. Li, C. Chen, Q. Li, X. J. Kong, Y. Liu, Z. Ji, S. Zou, M. Hong and M. Wu, An Ultra-stable Supramolecular Framework Based on Consecutive Side-by-side Hydrogen Bonds for One-step C_2H_4/C_2H_6 Separation, *Angew. Chem., Int. Ed.*, 2024, **63**, e202401754.

52 Y. Wang, K. Ma, J. Bai, T. Xu, W. Han, C. Wang, Z. Chen, K. O. Kirlikovali, P. Li, J. Xiao and O. K. Farha, Chemically Engineered Porous Molecular Coatings as Reactive Oxygen Species Generators and Reservoirs for Long-Lasting Self-Cleaning Textiles, *Angew. Chem., Int. Ed.*, 2022, **61**, e202115956.

53 J.-X. Wang, X. Zhang, C. Jiang, T.-F. Zhang, J. Pei, W. Zhou, T. Yildirim, B. Chen, G. Qian and B. Li, Construction of Highly Porous and Robust Hydrogen-Bonded Organic Framework for High-Capacity Clean Energy Gas Storage, *Angew. Chem., Int. Ed.*, 2024, **63**, e202411753.

54 M. Yi, S. Wang, S. Li, S. Zhang, Y. Liu, L. Zhang, Z. You, X. Liu, L. Li, J. Wang, H. Wang, Q. Zhao, B. Li and X.-H. Bu, Superhydrophobic Molecular Selector for Efficient Separation of Ethane over Ethylene under Dry and Humid Conditions, *J. Am. Chem. Soc.*, 2025, **147**, 13592–13600.

55 A. L. Spek, Single-crystal structure validation with the program PLATON, *J. Appl. Crystallogr.*, 2003, **36**, 7–13.

56 X. Zhang, L. Li, J.-X. Wang, H.-M. Wen, R. Krishna, H. Wu, W. Zhou, Z.-N. Chen, B. Li, G. Qian and B. Chen, Selective Ethane/Ethylene Separation in a Robust Microporous Hydrogen-Bonded Organic Framework, *J. Am. Chem. Soc.*, 2020, **142**, 633–640.

57 L. Zhang, Q. Lei, M. Yi, Z. Zhang, X. Lian, J. Xu, S. Zhang, L. Li, B. Li and X.-H. Bu, Bioinspired "Intermolecular Pocket" in Soft Molecular Crystal of Porous Organic Cage Exhibiting Reversible Guest Recognition, *Angew. Chem., Int. Ed.*, 2025, **64**, e202421753.

58 R.-B. Lin, H. Wu, L. Li, X.-L. Tang, Z. Li, J. Gao, H. Cui, W. Zhou and B. Chen, Boosting Ethane/Ethylene Separation within Isoreticular Ultramicroporous Metal–Organic Frameworks, *J. Am. Chem. Soc.*, 2018, **140**, 12940–12946.

59 P. Zhang, L. Yang, X. Liu, J. Wang, X. Suo, L. Chen, X. Cui and H. Xing, Ultramicroporous material based parallel and extended paraffin nano-trap for benchmark olefin purification, *Nat. Commun.*, 2022, **13**, 4928.

60 P. R. Spackman, M. J. Turner, J. J. McKinnon, S. K. Wolff, D. J. Grimwood, D. Jayatilaka and M. A. Spackman, CrystalExplorer: a program for Hirshfeld surface analysis, visualization and quantitative analysis of molecular crystals, *J. Appl. Crystallogr.*, 2021, **54**, 1006–1011.

61 S.-Y. Li, S.-C. Fan, P. Zhang, W.-Y. Yuan, Y. Wang and Q.-G. Zhai, Metal-cluster-powered ultramicropore alliance in pore-space-partitioned metal-organic frameworks for benchmark one-step ethylene purification, *Chem*, 2024, **10**, 2761–2775.

62 P.-Q. Liao, W.-X. Zhang, J.-P. Zhang and X.-M. Chen, Efficient purification of ethene by an ethane-trapping metal-organic framework, *Nat. Commun.*, 2015, **6**, 8697.

63 K.-J. Chen, D. G. Madden, S. Mukherjee, T. Pham, K. A. Forrest, A. Kumar, B. Space, J. Kong, Q.-Y. Zhang and M. J. Zaworotko, Synergistic sorbent separation for one-step ethylene purification from a four-component mixture, *Science*, 2019, **366**, 241–246.

64 L. Zhang, B. Yu, M. Wang, Y. Chen, Y. Wang, L.-B. Sun, Y.-B. Zhang, Z. Zhang, J. Li and L. Li, Ethane Triggered Gate-Opening in a Flexible-Robust Metal-Organic Framework for Ultra-High Purity Ethylene Purification, *Angew. Chem., Int. Ed.*, 2025, **64**, e202418853.

65 Y. Shi, Y. Xie, H. Cui, Y. Ye, H. Wu, W. Zhou, H. Arman, R.-B. Lin and B. Chen, Highly Selective Adsorption of Carbon Dioxide over Acetylene in an Ultramicroporous Metal–Organic Framework, *Adv. Mater.*, 2021, **33**, 2105880.

66 (*a*) CCDC 2425853: Experimental Crystal Structure Determination, 2026, DOI: 10.5517/ccdc.csd.cc2mf9bq; (*b*) CCDC 2425854: Experimental Crystal Structure Determination, 2026, DOI: 10.5517/ccdc.csd.cc2mf9cr; (*c*) CCDC 2425855: Experimental Crystal Structure Determination, 2026, DOI: 10.5517/ccdc.csd.cc2mf9ds; (*d*) CCDC 2425856: Experimental Crystal Structure Determination, 2026, DOI: 10.5517/ccdc.csd.cc2mf9ft; (*e*) CCDC 2425857: Experimental Crystal Structure Determination, 2026, DOI: 10.5517/ccdc.csd.cc2mf9gv; (*f*) CCDC 2425858: Experimental Crystal Structure Determination, 2026, DOI: 10.5517/ccdc.csd.cc2mf9hw.